Research Article Vol. 28, No. 12 / 8 June 2020 / Optics Express 17923

Optics EXPRESS

# Tuning the phase and amplitude response of plasmonic metasurface etalons

DANIELLE BEN HAIM,[1,2,*] LIOR MICHAELI,[1,2,3] ORI AVAYU,[1,2] AND TAL ELLENBOGEN[1,2]

[1] Department of Physical Electronics, School of Electrical Engineering, Tel-Aviv University, Tel Aviv 6997801, Israel
[2] Center for Light-Matter Interaction, Tel-Aviv University, Tel-Aviv 6779801, Israel
[3] Raymond and Beverly Sackler School of Physics & Astronomy, Tel-Aviv University, Tel-Aviv 6779801, Israel
[*] benhaim.danielle@gmail.com

**Abstract:** We study the optical response of plasmonic metasurface etalons in reflection. The etalons consist of a metallic mirror and a plasmonic metasurface separated by wavelength-scale dielectric spacer. We show that tuning the localized surface plasmon resonance and spacer thickness can be used to achieve both enhanced reflectivity and perfect absorption, in addition to full $2\pi$ range phase control, and tunable regions of normal and anomalous dispersion. We validate our claims by measuring the spectral reflection and phase response of metasurface etalons consisting aluminum nanodisks of different radii separated from an aluminum reflector by a $SiO_2$ spacer. In addition, we use this approach to demonstrate a simple Hermite-Gaussian (HG) wavelength selective beam-shaping reflective mask. The concept can be further extended by using multilayers to obtain multi-functional elements.

## 1. Introduction

Plasmonic metasurfaces are planar, usually subwavelength spaced, arrays of metallic particles that exhibit resonant scattering at their localized surface plasmon resonance (LSPR). They drew a great amount of attention over the past years due to their ability to control and manipulate light in planar platforms, having prominent potential to form unique and integrated optical elements. Various applications based on plasmonic metasurfaces have been demonstrated recently, including wavefront control, mode conversion, focusing, holography and polarization control, as well as frequency conversion, strong coupling with excitons, and lasing [1–15].

The working principle of plasmonic metasurfaces lies in the strong interaction between the electromagnetic field and the free electrons on the surface of the metallic nanoparticles around the LSPR. This resonant interaction gives rise to strong scattering and local field enhancements that are utilized in the different applications of plasmonic metasurfaces. One of the most attractive features of plasmonic metasurfaces is that their specific spectral and polarization response can be easily tuned, by controlling the shape and size of the metallic nanoparticles.

However, realizing highly transmissive plasmonic metasurfaces proved challenging due to their relatively strong scattering, in addition to their phase response that is limited to $\pi$ range around the resonance. Nevertheless, when incorporating plasmonic metasurfaces with back-reflectors, it is possible to achieve both high reflectivity and full $2\pi$ range phase control. Different types of reflective plasmonic metasurfaces have been extensively researched, introducing the concept of gap surface plasmons [16–18], exciting hot spots [19], exhibiting perfect absorption [20–23] and beam steering [24,25], holograms [12,13], metalenses [26,27] and color printing [28,29]. Their underlying physics has been explored, examining the influence of different parameters, such as the spacer thickness, array period, incidence angle and particle shape, on the plasmonic modes and the reflected field [17,23,26,30–35].

#392520 https://doi.org/10.1364/OE.392520
Journal © 2020 Received 10 Mar 2020; revised 4 May 2020; accepted 5 May 2020; published 1 Jun 2020

In this work we focus on plasmonic etalon type metasurfaces, and study how to engineer their phase and amplitude response by simultaneously controlling the etalon thickness and nanoantenna size and shape. We show that the coupling between Fabry-Perot resonances in the system and the LSPR of the nanoantennas plays a major role in the optical response. When varying the radius size of the nanoantennas, we observe splitting of the LSPR into pairs of resonant modes, expressed by perfect absorption and accompanied by phase singularities. A similar behavior which originate from the same phenomenon was recently reported and analyzed by Berkhout and Koenderink [23]. We further show that the spacer thickness is of great importance to the design, since it provides control over the density of the resonances in the spectral bandwidth. This in consequence impacts their width and strength and the spectral regions of normal and anomalous phase response. We study the system by finite-difference-time-domain (FDTD) electromagnetic simulations (Lumerical FDTD) and compare to experimental results measured from fabricated samples with different nanoantenna radii. The numerical and experimental results agree well and provide a strong support for our claims. Finally, we also demonstrate a wavelength selective reflective mode converter to show the potential of the design for beam-shaping applications and discuss further implementations and possibilities.

## 2. Theoretical analysis

The studied reflective metasurface consists of a layer of aluminum plasmonic nanoantenna array, an aluminum mirror and a glass spacer that separates between them. A schematic illustration of the structure is demonstrated in Fig. 1(a).

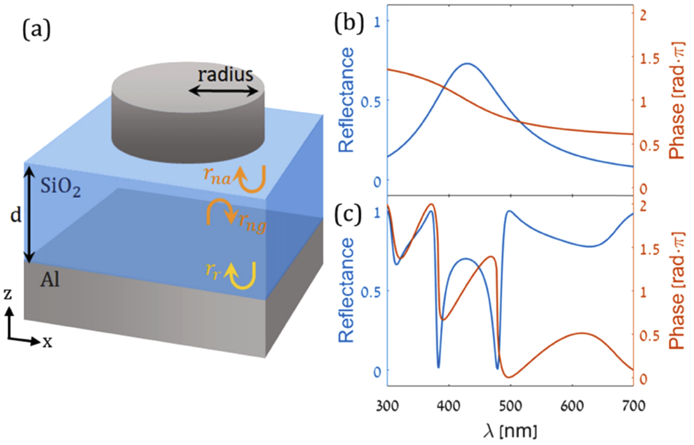

**Fig. 1.** (a) Schematic illustration of a single unit cell of the periodic structure. The structure consists of 3 layers: 40nm thick aluminum nanodisk array, $SiO_2$ spacer of varying thickness d and 200nm thick aluminum layer. (b) Theoretical reflectance and phase response of a plasmonic metasurface, modeled by a Lorentzian function. The resonance parameters are taken from FDTD simulation of aluminum nanodisks metasurface (radius 70nm, thickness 40nm, side-to-side disk separation 120nm) placed on $SiO_2$ substrate. (c) Theoretical reflectance and phase response of the plasmonic metasurface in (b) placed on a $SiO_2$ spacer with d=510nm over a perfect mirror.

To describe the response of the thin plasmonic array we first assume a simplified case of an infinite array of non-interacting metallic nanoparticles. The polarizability of each nanoparticle is described by a Lorentzian lineshape [36,37] and their corresponding reflection and transmission coefficients are [38,39]:

$$\begin{aligned} r &= \mathrm{A}\frac{i\gamma\omega}{\omega_0^2-\omega^2-i\gamma\omega} \\ t &= 1+r, \end{aligned} \tag{1}$$

where $\omega$ is the frequency, $\omega_0$ and $\gamma$ are the resonance frequency and its width respectively, and A is a parameter set to describe the resonance strength. The calculated reflection coefficient of a plasmonic metasurface composed of aluminum nanodisks with radius 70nm, thickness 40nm, and side-to-side disk separation 120nm, placed on $SiO_2$ substrate, is portrayed in Fig. 1(b). In the calculation, the resonance parameters $\omega_0$ and $\gamma$ were taken from FDTD simulation of the system. It can be seen that the reflectance $|r|^2$ features a peak at the LSPR wavelength together with a π phase transition around it. Tuning the resonance frequency $\omega_0$ is possible by changing the size of the nanoantennas. In the case of metallic particles, increasing their size will result in red-shift, as well as broadening of the LSPR [40].

To obtain the reflected field from the entire structure shown in Fig. 1(a), including the plasmonic array, $SiO_2$ spacer and aluminum reflector, we consider a Fabry-Perot model. The total reflection coefficient from the structure is:

$$r_{tot} = \frac{r_{na} + (r_{na} + r_{ng} + 1)r_r \exp\left(i\frac{4\pi \mathrm{d} n_s}{\lambda}\right)}{1 - r_{ng} r_r \exp\left(i\frac{4\pi \mathrm{d} n_s}{\lambda}\right)}, \tag{2}$$

where $r_{na}$ and $r_{ng}$ are the reflection coefficients for wave incident from air and glass, respectively, $r_r$ is the reflection coefficient of the reflector, $n_s$ is the spacer refractive index, d is the spacer thickness and $\lambda$ is the wavelength. The phase term appears in the numerator and denominator of Eq. (2) is associated with the Fabry–Perot resonances, which appear periodically with $2\mathrm{d}n_s/\lambda$. Although the expression in Eq. (2) considers an infinite array and neglects inter-particle coupling effects, it still reveals the basic phenomena that take place in the structure. As opposed to the single LSPR mode observed in the nanoantenna array, in the combined structure several resonant modes arise, as explicitly demonstrated in Fig. 1(c). Very interestingly, it can be seen that the emergence of these modes is accompanied with regions of near perfect absorption, phase modulation of full 2π range, and areas of normal and anomalous phase dispersion. Therefore, it is highly important to explore the ability to control these regions and their application for optical manipulation.

A phenomenological approach can be taken to describe these modes as originating from coupling between the LSPR and the Fabry–Perot resonances. As will be later shown, each mutual occurrence of Fabry–Perot resonance and LSPR, may lead under specific conditions, to such coupling and splitting into two modes, one lower and one higher in frequency.

Since the new modes emerge from the interaction between the LSPR and the Fabry-Perot resonances of the system, tuning the coupling parameters allows to control the aforementioned effects associated with the coupling. It can be shown that under sufficiently strong coupling [23] the perfect absorption conditions occur at a pair of wavelengths, lower and higher than the LSPR. This condition requires the elimination of the numerator of Eq. (2), which happens when the amplitudes of the different terms in the numerator satisfy $|r_{na}| = |r_{na} + r_{ng} + 1||r_r|$. This yields the two wavelengths at which perfect absorption can occur, $\lambda_l$ and $\lambda_h$, for the lower and higher wavelength, respectively. Since this condition depends only on the reflection coefficients it can be tuned by controlling the LSPR properties. The relative phase of the numerator terms connects between the two wavelengths and the corresponding spacer thickness values that support the perfect absorption condition. Once the wavelengths are obtained, the phase term $\exp(i4\pi \mathrm{d}n_s/\lambda)$ is tuned by the spacer thickness d to achieve the perfect absorption condition. It follows that each wavelength will correspond to a different thickness value, but the two conditions will still be inherently connected to each other as a pair of splitted resonances that originate from the same mode. The pairs of resonances will be repeated periodically, where each pair is related to a distinct Fabry-Perot mode. A connection between the two wavelengths and the corresponding d values can be obtained by noticing the symmetrical properties of the Lorentzian based reflection coefficient in Eq. (1), which leads to the following relation:

$$n_s\left(\frac{d_{l,m}}{\lambda_l}+\frac{d_{h,m}}{\lambda_h}\right)=\frac{1}{2}+m, \qquad m=0,1,2,\ldots, \tag{3}$$

where d$_{l,m}$ and d$_{h,m}$ correspond to $\lambda_l$ and $\lambda_h$, respectively, and the index m stands for the mode of the pair.

The validity of the model above breaks at lower wavelengths since it excludes the diffraction orders that originate from the structure periodicity. These diffraction modes can excite in turn new confined modes of the system, such as propagating surface plasmon modes on the interface of the metal and waveguide modes propagating inside the spacer. For the case of normal incidence, waveguide modes will appear at wavelengths below the first Rayleigh anomaly [41] and they can be found according to the following self-consistency condition:

$$\frac{2\pi}{\lambda}n_s 2\mathrm{d}\cos\theta_p+\varphi_{r_{ng}}+\varphi_{r_r}=2\pi p, \qquad p=0,1,2,\ldots, \tag{4}$$

where $\varphi_{r_{ng}}$ and $\varphi_{r_r}$ are the phases of the reflection coefficients $r_{ng}$ and $r_r$, respectively, $\theta_p=\sin^{-1}(p\lambda/n_s\Lambda)$ is the diffraction angle, corresponding to the p$^{\text{th}}$ waveguide mode, with respect to the normal to the interface, and $\Lambda$ is the array period. Such confined modes have been recently demonstrated in a transmissive metasurface as well [42]. As will be shown later, this interaction will also have significant influence on the zero-order reflected wave.

## 3. Results

To demonstrate experimentally and by simulations the capability of the structure presented above to control the amplitude and phase of the reflected field, we fabricated a corresponding sample composed of 3 layers. The top and bottom layers consisted of square array of 40nm thick aluminum disk-shaped nanoantennas, and 200nm thick aluminum reflector, respectively, separated by a SiO$_2$ spacer layer. Schematic illustration of this sample is depicted in Fig. 1(a). The separation between the nanodisks was chosen to achieve the desired splitting into two resonances, as mentioned before.

First, we preformed FDTD simulations of the entire structure. Periodic boundary conditions were applied, and the complex reflected field was extracted. To examine the tuning effects, the simulations were performed for a range of nanodisk radii and spacer thicknesses. We point out that in contrast to the theoretical model, the full-wave FDTD simulations take into consideration interband transition and absorption in the metal particles and reflector, as well as evanescent waves, near-field interactions and diffraction effects, as previously discussed.

In Figs. 2(a) and 2(b) we show the relative reflected intensity and phase, respectively, obtained from the FDTD simulations as function of the spacer thickness d and wavelength λ for fixed nanodisks radius of 70nm. The relative reflected intensity and phase were obtained by normalizing the reflection from the entire structure with the reflection from the structure without the metasurface on top.

It can be seen that, in agreement to the theoretical predictions above, the reflectivity exhibits pairs of absorption dips, at $\lambda_l{\approx}390$nm and $\lambda_h{\approx}480$nm, surrounding the spectral location of the LSPR, marked by the white dashed line. The reflected intensity from the 3 layer system reaches a maximum of 0.92, which makes the relative reflected intensity reach a maximum of 1.05. This maximum intensity appears in lines that follow the Fabry–Perot periodicity of the system, marked by black dashed lines, according to the exponential term in Eq. (2). Each pair of associated

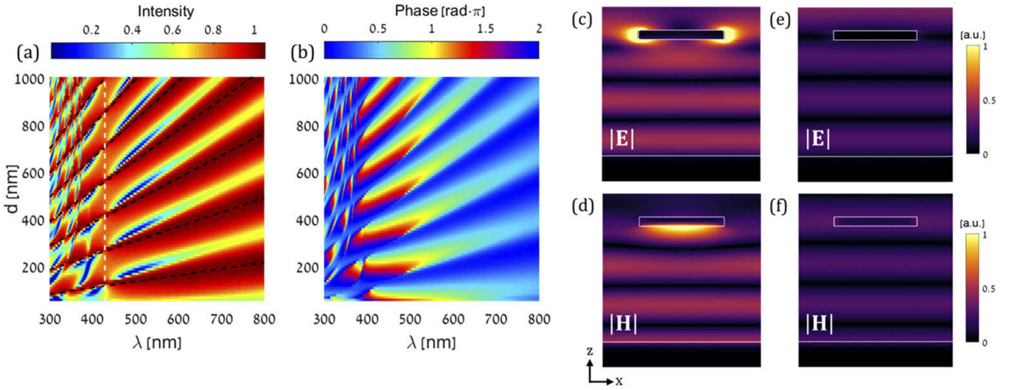

**Fig. 2.** FDTD simulation results of the relative reflected (a) intensity and (b) phase from a structure consisting disks with radius of 70nm and side-to-side separation of 120nm as function of λ and d. The white line marks the LSPR of the nanodisks array and the black lines mark the maximum reflected intensity corresponding to the Fabry-Perot periodicity. (c-d) Normalized electric and magnetic fields distribution at λ=496nm, near perfect absorption, and (e-f) at λ=515nm, the maximum reflected intensity, respectively, for d=500nm.

perfect absorption dips is bound between two such lines. Figures 2(c)–2(d) and 2(e)–2(f) show the electric and magnetic fields distribution near a perfect absorption dip and at a maximum reflected intensity peak, respectively. A pronounced enhancement of the local field around the nanodisk can be seen at the resonant mode, as opposed to the transparency of the nanodisks array that is seen at the reflected intensity peak.

The perfect absorption condition origins from zero of the scattering matrix, as explained in [43]. This condition is accompanied by phase singularity, which can be seen in Fig. 2(b), as was also discussed before in [44,45]. Examining the phase of the reflected field shows that each pair of perfect absorption points is related to opposite residue charges of ±1, as discussed extensively in [23]. It can be seen in the full electromagnetic simulations results that below the first Rayleigh anomaly wavelength, at $\lambda < n_s \Lambda$=380nm, new modes appear, as described before, which clearly show a significant effect on the zero-order reflection. The theoretical model leading to Eq. (2) can yield similar results to those shown in Figs. 2(a) and 2(b), however they will not attest to the existence of the confined modes.

Tuning the nanodisk radius modifies the LSPR location which in turn translates into moving the entire pattern shown in Fig. 2 along the wavelength axis. The reflected intensity and phase as function of radius and wavelength, for 3 different spacer thicknesses, d=300nm, d=600nm, and d=1000nm, are presented in Figs. 3(a)–3(b), 3(c)–3(d) and 3(e)–3(f), respectively. It can be seen that also in this parameter space, perfect absorption points are accompanied with phase singularities. Figure 3(g) shows the reflected intensity and phase at λ=544nm, for d=600nm, where it can be seen that by tuning the radius, almost 2π phase change can be achieved, with reflected intensity values higher than 0.6. By increasing the spacer thickness, the wavelength of perfect absorption can be further tuned, and more coupled modes appear with sharper resonant features. Finally, since the array period Λ is increasing with the radius, so does the Rayleigh anomaly wavelength, thus the region of waveguide modes takes a larger part in the parameters space.

In order to validate the simulations results, 16 arrays of aluminum nanodisks (50µm×50µm each), with increasing disk radii were tested. To fabricate the sample, a 200nm layer of aluminum was evaporated on a glass substrate (e-beam evaporation). Then, a 600nm layer of $SiO_2$ was grown on top of it (plasma enhanced chemical vapor deposition - PECVD). After spin coating

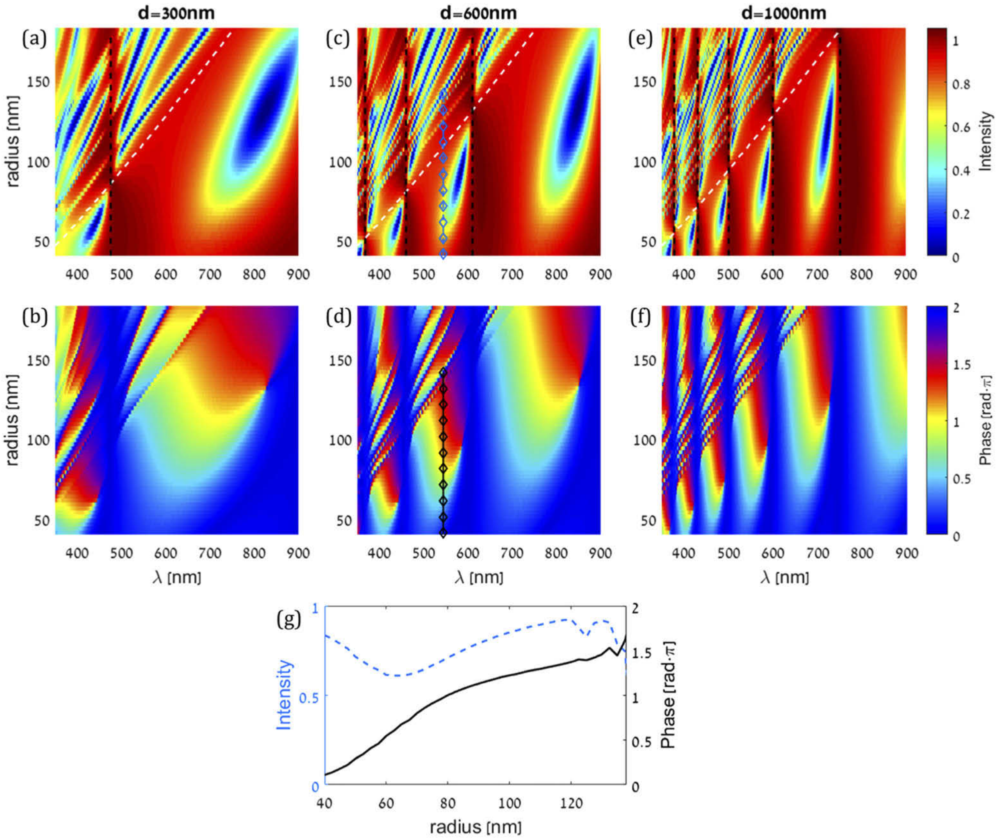

**Fig. 3.** FDTD simulation results of the relative reflected intensity and phase, comparing 3 different spacer thicknesses: (a-b) d=300nm, (c-d) 600nm and (e-f) 1000nm, as function of radius and λ. The white lines mark the LSPR of the nanodisks array and the black lines mark the maximum reflected intensity corresponding to the Fabry-Perot periodicity. (g) Cross-section of the relative reflected intensity and phase for d=600nm at λ=544nm, as marked in (c) and (d) by the blue and black markers, respectively.

e-beam resist (PMMA A4) on top of the $SiO_2$, the pattern of the nanodisks arrays was written using e-beam lithography (Raith 150-2). After developing the resist, a 40nm aluminum film was evaporated (e-beam evaporation), followed by a lift-off process. The final device therefore consists of a reflector layer of 200nm aluminum, a spacer layer of 600nm $SiO_2$ and 40nm thick aluminum nanodisks arrays placed on top of the spacer.

The samples were characterized in an optical interferometric microscopy spectral phase characterization setup [46]. The sample was illuminated by a collimated beam (NKT SuperK Compact), with an angle divergence of less than 1 degree, which enabled observing the reflected modes of the structure. The measurements were normalized with respect to a reference plane, which in our case was the substrate area without the nanodisks, but with the buried reflector.

In Fig. 4 we present the relative reflected intensity and phase, extracted from the experiment (Figs. 4(a) and 4(b)) and simulations (Figs. 4(c) and 4(d)). Figures 4(a) and 4(c) show the relative intensity while Figs. 4(b) and 4(d) show the relative phase. It can be seen that there is a good agreement between the experimental results and the simulations. The reflection spectra feature the same modes as the simulations, including the locations of strong absorption dips with associated phase singularities, high reflection areas, as well as some of the narrow features related to the waveguide modes. The relative phase results show the similar distribution between each pair of dips that enables tuning over the entire 2π range by choosing the desired radius size. This property opens the opportunity to create spatially varying amplitude and phase masks to modulate the reflected wavefront.

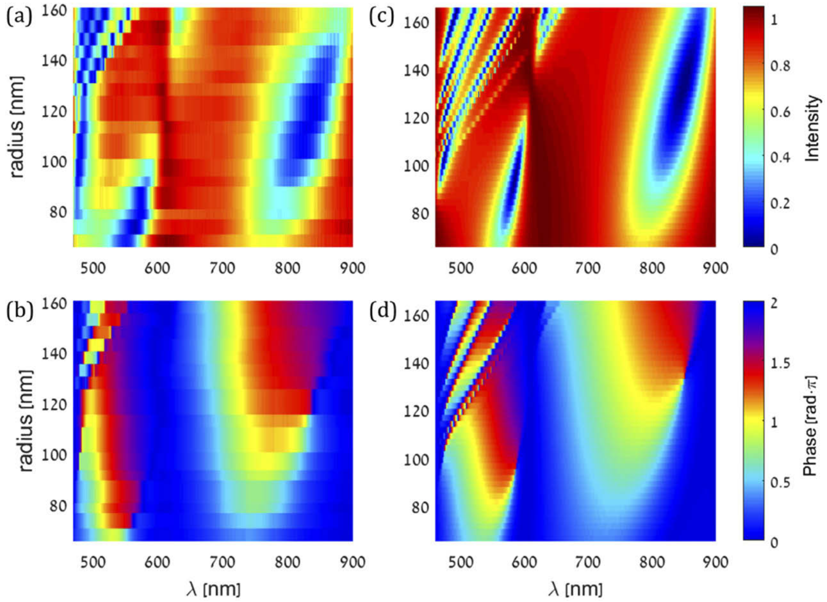

**Fig. 4.** Experimental reflected intensity (a) and phase (b) and corresponding simulation results (c) and (d) respectively. The measurement was taken from 16 samples of disks with different radii and spacer thickness of d=600nm.

To demonstrate the capability of the studied metasurface etalons for wavefront shaping, we use it to implement a frequency selective reflective mode converter of a Gaussian beam into a first order Hermite-Gaussian (HG10). A simple element that can transform with good efficiency an illuminated Gaussian beam into an HG10 corresponds to a binary phase mask of 0 and π. To implement the mode converter, the desired points of reflection and phase need to be chosen in the parameter space spanned by the disk radius and spacer thickness. For the fabricated sample with spacer thickness of d=600nm we chose nanodisk radius of 145nm that shows the desired selective functionality. Specifically it exhibits relative π phase shift at λ=728nm, and 0 phase shift at 600nm, while maintaining reflection intensity close to 1, as can be seen in Fig. 4. Illuminating the sample with a Gaussian beam incident on the boundary between the sample and the reference exerts the desired phase difference resulting in selectively converting the beam only at λ=728nm. Figures 5(a), 5(b), (5(c) and 5(d)) show the image of the beam at λ=728nm (λ=600nm) on the sample and in the far field, respectively. The selective mode conversion for λ=728nm is evident.

This demonstration is only one example of the vast possibilities of wavefront modulation that is achievable using this method. The values of the phase map show that sequential phase modulation is possible as well by using nanodisks of different sizes, when treating them as building blocks that can be placed accordingly to construct any desired mask. In this reflective structure, the spacer thickness serves as an additional parameter that has a major impact on the spectral response of the nanodisks and should be chosen accordingly. As was previously shown, the tuning of the spacer thickness controls the working bandwidth, to be either broad or narrow, and also enables multi-frequency operation.

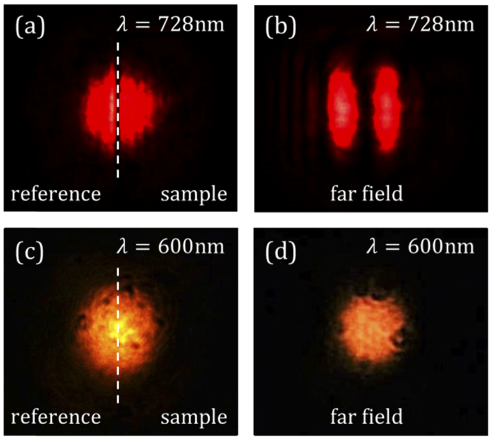

**Fig. 5.** Selective binary HG10 beam-shaping by a sample with radius≅145nm illuminated by a Gaussian beam. Measurements at wavelength λ=728nm (a-b), where the beam-shaping occurs, and at wavelength λ=600nm (c-d), where there is no modulation. Images of the sample (a,c) and far-field (b,d).

To realize the concept of sequential phase modulation we design an optical element based on our reflective structure, constructed from nanodisks of different radii, tailored to achieve the desired phase response. Specifically, we use the simulation results from Fig. 3(g) to form a metalens (metasurface-based lens) with 200µm diameter and 1mm focal length that operates at λ=544nm. We discretized the phase as a function of the radius, as shown in Fig. 6(a), and used it to map the lens phase profile to the corresponding radius of the nanodisk that should be placed at each location on the surface. The phase response of the designed metalens is shown in Fig. 6(b). To simulate the focal point we used a beam propagation simulation (Matlab) based on the transfer function in free space and plane wave illumination [47]. The light at the focal point presented in Fig. 6(c) was focused with efficiency of 74.6%.

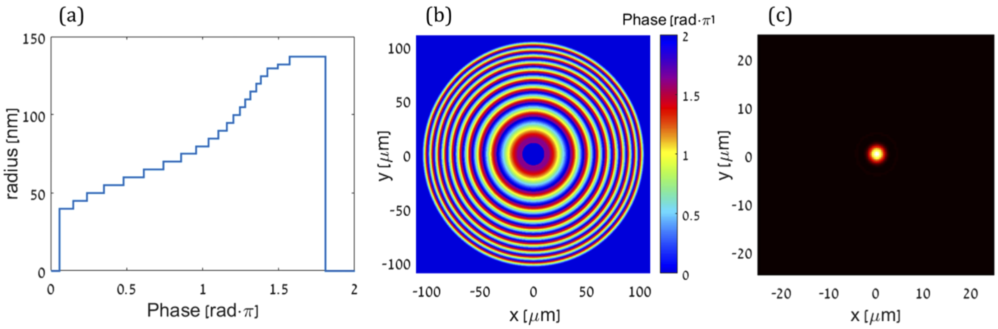

**Fig. 6.** Realization of a metalens. (a) Mapping of the phase response to nanodisk radius, according to the simulation results from Fig. 3(g). (b) The phase of a metalens designed to a focal length of 1mm at λ=544nm. (c) Numerical calculation of the focal spot using beam propagation simulation.

## 4. Conclusions

We have demonstrated the capability of reflective plasmonic metasurface etalons to control the amplitude and phase of reflected light. We showed that strong interaction between the LSPR of the nanodisks and the Fabry-Perot resonances of the etalon gives rise to pairs of coupled resonances, which enable the entire $2\pi$ phase control. The ability to tune and control the appearance of these coupled resonances was studied, by separately tuning the LSP and Fabry-Perot parameters. The tuning of the nanodisk radius and the spacer thickness allows full control over the amplitude and phase of the reflected light and the regions of normal and anomalous phase dispersion. In addition, it also affects the region of confined modes of the structure, which can be of interest due to the very narrow features in both amplitude and phase. These modes can be further investigated by introducing the coupled-dipole approximation summation method. The understanding of the tunable phase and amplitude response allowed us also to present experimentally an approach for selective beam shaping using the structure, and numerically a metalens design reaching almost 75% efficiency. This approach can be implemented in various optical applications.

The studied configuration exhibits phenomena that relies on the LSP and the Fabry-Perot etalon properties. Thus, it can be extended to incorporate any type and shape of plasmonic nanoantennas that exhibit LSPR, e.g. nanorods, to achieve polarization dependent operation, and can also be also used to enhance the nonlinear generation in nanoantennas that exhibit nonlinear response [15,48].

The metasurface etalon concept can be further extended to multiplex several independent functionalities by incorporating more layers to the design. A theoretical model of the multilayer design can be formulated using the wave-transfer matrix method, where each layer is treated separately, independent of the other layers. This is a good approximation when the distance between the layers is of scale $\sim\lambda$. Using different metals for each metasurface layer can also reduce the crosstalk between them. Another approach can use high index dielectric nanoparticles to reduce losses and enhance the performance. Altogether, we believe that this can be very interesting system for implementation of thin, multifunctional and integrated optical elements, for a wide range of applications.

## Funding

Ministry of Science, Technology and Space (3-15614); Israel Science Foundation (581/19).

## Acknowledgments

D. Ben Haim acknowledges the scholarship for excellent students given by the Iby and Aladar Fleischman Faculty of Engineering at Tel-Aviv University.

## Disclosures

The authors declare no conflicts of interest.

## References

1. F. Monticone, N. M. Estakhri, and A. Alù, "Full control of nanoscale optical transmission with a composite metascreen," Phys. Rev. Lett. **110**(20), 203903 (2013).
2. N. Yu, P. Genevet, M. A. Kats, F. Aieta, J. P. Tetienne, F. Capasso, and Z. Gaburro, "Light propagation with phase discontinuities: Generalized laws of reflection and refraction," Science **334**(6054), 333–337 (2011).
3. S. Keren-Zur, O. Avayu, L. Michaeli, and T. Ellenbogen, "Nonlinear Beam Shaping with Plasmonic Metasurfaces," ACS Photonics **3**(1), 117–123 (2016).
4. A. E. Schlather, N. Large, A. S. Urban, P. Nordlander, and N. J. Halas, "Near-field mediated plexcitonic coupling and giant Rabi splitting in individual metallic dimers," Nano Lett. **13**(7), 3281–3286 (2013).
5. E. Eizner, O. Avayu, R. Ditcovski, and T. Ellenbogen, "Aluminum Nanoantenna Complexes for Strong Coupling between Excitons and Localized Surface Plasmons," Nano Lett. **15**(9), 6215–6221 (2015).
6. T. K. Hakala, H. T. Rekola, A. I. Väkeväinen, J. P. Martikainen, M. Nečada, A. J. Moilanen, and P. Törmä, "Lasing in dark and bright modes of a finite-sized plasmonic lattice," Nat. Commun. **8**(1), 13687 (2017).
7. A. Yang, T. B. Hoang, M. Dridi, C. Deeb, M. H. Mikkelsen, G. C. Schatz, and T. W. Odom, "Real-time tunable lasing from plasmonic nanocavity arrays," Nat. Commun. **6**(1), 6939 (2015).

8. E. Karimi, S. A. Schulz, I. De Leon, H. Qassim, J. Upham, and R. W. Boyd, “Generating optical orbital angular momentum at visible wavelengths using a plasmonic metasurface,” Light: Sci. Appl. **3**(5), e167 (2014).
9. O. Avayu, E. Almeida, Y. Prior, and T. Ellenbogen, “Composite functional metasurfaces for multispectral achromatic optics,” Nat. Commun. **8**(1), 14992 (2017).
10. M. Khorasaninejad, W. T. Chen, R. C. Devlin, J. Oh, A. Y. Zhu, and F. Capasso, “Metalenses at visible wavelengths: Diffraction-limited focusing and subwavelength resolution imaging,” Science **352**(6290), 1190–1194 (2016).
11. L. Huang, X. Chen, H. Mühlenbernd, H. Zhang, S. Chen, B. Bai, Q. Tan, G. Jin, K. W. Cheah, C. W. Qiu, J. Li, T. Zentgraf, and S. Zhang, “Three-dimensional optical holography using a plasmonic metasurface,” Nat. Commun. **4**(1), 2808 (2013).
12. G. Zheng, H. Mühlenbernd, M. Kenney, G. Li, T. Zentgraf, and S. Zhang, “Metasurface holograms reaching 80% efficiency,” Nat. Nanotechnol. **10**(4), 308–312 (2015).
13. Y. W. Huang, W. T. Chen, W. Y. Tsai, P. C. Wu, C. M. Wang, G. Sun, and D. P. Tsai, “Aluminum plasmonic multicolor meta-Hologram,” Nano Lett. **15**(5), 3122–3127 (2015).
14. F. Aieta, P. Genevet, N. Yu, M. A. Kats, Z. Gaburro, and F. Capasso, “Out-of-plane reflection and refraction of light by anisotropic optical antenna metasurfaces with phase discontinuities,” Nano Lett. **12**(3), 1702–1706 (2012).
15. N. Segal, S. Keren-Zur, N. Hendler, and T. Ellenbogen, “Controlling light with metamaterial-based nonlinear photonic crystals,” Nat. Photonics **9**(3), 180–184 (2015).
16. M. G. Nielsen, A. Pors, O. Albrektsen, and S. I. Bozhevolnyi, “Efficient absorption of visible radiation by gap plasmon resonators,” Opt. Express **20**(12), 13311 (2012).
17. A. Pors and S. I. Bozhevolnyi, “Plasmonic metasurfaces for efficient phase control in reflection,” Opt. Express **21**(22), 27438 (2013).
18. F. Ding, Y. Yang, R. A. Deshpande, and S. I. Bozhevolnyi, “A review of gap-surface plasmon metasurfaces: Fundamentals and applications,” Nanophotonics **7**(6), 1129–1156 (2018).
19. H. Harutyunyan, A. B. F. Martinson, D. Rosenmann, L. K. Khorashad, L. V. Besteiro, A. O. Govorov, and G. P. Wiederrecht, “Anomalous ultrafast dynamics of hot plasmonic electrons in nanostructures with hot spots,” Nat. Nanotechnol. **10**(9), 770–774 (2015).
20. N. Liu, M. Mesch, T. Weiss, M. Hentschel, and H. Giessen, “Infrared perfect absorber and its application as plasmonic sensor,” Nano Lett. **10**(7), 2342–2348 (2010).
21. H. T. Chen, “Interference theory of metamaterial perfect absorbers,” Opt. Express **20**(7), 7165 (2012).
22. Y. Yao, R. Shankar, M. A. Kats, Y. Song, J. Kong, M. Loncar, and F. Capasso, “Electrically tunable metasurface perfect absorbers for ultrathin mid-infrared optical modulators,” Nano Lett. **14**(11), 6526–6532 (2014).
23. A. Berkhout and A. F. Koenderink, “Perfect Absorption and Phase Singularities in Plasmon Antenna Array Etalons,” ACS Photonics **6**(11), 2917–2925 (2019).
24. S. Sun, K. Y. Yang, C. M. Wang, T. K. Juan, W. T. Chen, C. Y. Liao, Q. He, S. Xiao, W. T. Kung, G. Y. Guo, L. Zhou, and D. P. Tsai, “High-efficiency broadband anomalous reflection by gradient meta-surfaces,” Nano Lett. **12**(12), 6223–6229 (2012).
25. A. Pors, O. Albrektsen, I. P. Radko, and S. I. Bozhevolnyi, “Gap plasmon-based metasurfaces for total control of reflected light,” Sci. Rep. **3**(1), 2155 (2013).
26. S. Zhang, M. H. Kim, F. Aieta, A. She, T. Mansuripur, I. Gabay, M. Khorasaninejad, D. Rousso, X. Wang, M. Troccoli, N. Yu, and F. Capasso, “High efficiency near diffraction-limited mid-infrared flat lenses based on metasurface reflectarrays,” Opt. Express **24**(16), 18024–18034 (2016).
27. S. Wang, P. C. Wu, V. C. Su, Y. C. Lai, C. Hung Chu, J. W. Chen, S. H. Lu, J. Chen, B. Xu, C. H. Kuan, T. Li, S. Zhu, and D. P. Tsai, “Broadband achromatic optical metasurface devices,” Nat. Commun. **8**(1), 187 (2017).
28. F. Cheng, J. Gao, S. T. Luk, and X. Yang, “Structural color printing based on plasmonic metasurfaces of perfect light absorption,” Sci. Rep. **5**(1), 11045 (2015).
29. A. S. Roberts, S. M. Novikov, Y. Yang, Y. Chen, S. Boroviks, J. Beermann, N. A. Mortensen, and S. I. Bozhevolnyi, “Laser Writing of Bright Colors on Near-Percolation Plasmonic Reflector Arrays,” ACS Nano **13**(1), 71–77 (2019).
30. A. Christ, T. Zentgraf, S. G. Tikhodeev, N. A. Gippius, J. Kuhl, and H. Giessen, “Controlling the interaction between localized and delocalized surface plasmon modes: Experiment and numerical calculations,” Phys. Rev. B: Condens. Matter Mater. Phys. **74**(15), 155435 (2006).
31. R. Ameling and H. Giessen, “Microcavity plasmonics: Strong coupling of photonic cavities and plasmons,” Laser Photonics Rev. **7**(2), 141–169 (2013).
32. C. Qu, S. Ma, J. Hao, M. Qiu, X. Li, S. Xiao, Z. Miao, N. Dai, Q. He, S. Sun, and L. Zhou, “Tailor the Functionalities of Metasurfaces Based on a Complete Phase Diagram,” Phys. Rev. Lett. **115**(23), 235503 (2015).
33. A. Kwadrin, C. I. Osorio, and A. F. Koenderink, “Backaction in metasurface etalons,” Phys. Rev. B **93**(10), 104301 (2016).
34. R. Alaee, M. Albooyeh, and C. Rockstuhl, “Theory of metasurface based perfect absorbers,” J. Phys. D: Appl. Phys. **50**(50), 503002 (2017).
35. A. E. Minovich and A. V. Zayats, “Geometric-Phase Metasurfaces Based on Anisotropic Reflection: Generalized Design Rules,” ACS Photonics **5**(5), 1755–1761 (2018).
36. I. Zorić, M. Zäch, B. Kasemo, and C. Langhammer, “Gold, platinum, and aluminum nanodisk plasmons: Material independence, subradiance, and damping mechanisms,” ACS Nano **5**(4), 2535–2546 (2011).

37. M. Decker, I. Staude, M. Falkner, J. Dominguez, D. N. Neshev, I. Brener, T. Pertsch, and Y. S. Kivshar, “High-Efficiency Dielectric Huygens’ Surfaces,” Adv. Opt. Mater. **3**(6), 813–820 (2015).
38. F. J. G. De Abajo, “Colloquium: Light scattering by particle and hole arrays,” Rev. Mod. Phys. **79**(4), 1267–1290 (2007).
39. A. B. Evlyukhin, C. Reinhardt, A. Seidel, B. S. Luk’Yanchuk, and B. N. Chichkov, “Optical response features of Si-nanoparticle arrays,” Phys. Rev. B: Condens. Matter Mater. Phys. **82**(4), 045404 (2010).
40. S. A. Maier, *Plasmonics: Fundamentals and Applications* (Springer, 2007).
41. L. Rayleigh, “On the dynamical theory of gratings,” Proc. R. Soc. Lond. A **79**(532), 399–416 (1907).
42. O. Reshef, M. Saad-Bin-Alam, M. J. Huttunen, G. Carlow, B. T. Sullivan, J. M. Ménard, K. Dolgaleva, and R. W. Boyd, “Multiresonant High- Q Plasmonic Metasurfaces,” Nano Lett. **19**(9), 6429–6434 (2019).
43. A. Krasnok, D. Baranov, H. Li, M. A. Miri, F. Monticone, and A. Alú, “Anomalies in light scattering,” Adv. Opt. Photonics **11**(4), 892 (2019).
44. V. G. Kravets, F. Schedin, R. Jalil, L. Britnell, R. V. Gorbachev, D. Ansell, B. Thackray, K. S. Novoselov, A. K. Geim, A. V. Kabashin, and A. N. Grigorenko, “Singular phase nano-optics in plasmonic metamaterials for label-free single-molecule detection,” Nat. Mater. **12**(4), 304–309 (2013).
45. K. V. Sreekanth, S. Sreejith, S. Han, A. Mishra, X. Chen, H. Sun, C. T. Lim, and R. Singh, “Biosensing with the singular phase of an ultrathin metal-dielectric nanophotonic cavity,” Nat. Commun. **9**(1), 369 (2018).
46. L. Michaeli, D. Ben Haim, M. Sharma, H. Suchowski, and T. Ellenbogen, “Spectral Interferometric Microscopy for Fast and Broadband Phase Characterization,” *Adv. Opt. Mater.*, In press (2020).
47. B. E. A. Saleh and M. C. Teich, *Fundamentals of Photonics* (Wiley, 2007).
48. L. Michaeli, S. Keren-Zur, O. Avayu, H. Suchowski, and T. Ellenbogen, “Nonlinear Surface Lattice Resonance in Plasmonic Nanoparticle Arrays,” Phys. Rev. Lett. **118**(24), 243904 (2017).